Transmission spectroscopy of the inflated exoplanet WASP-52b, and evidence for a bright region on the stellar surface

J. Kirk,[1][*] P. J. Wheatley,[1] T. Louden,[1] S. P. Littlefair,[2] C. M. Copperwheat,[3] D. J. Armstrong,[1,4] T. R. Marsh[1] and V. S. Dhillon[2,5]

[1]*Department of Physics, University of Warwick, Coventry CV4 7AL, UK*
[2]*Department of Physics and Astronomy, University of Sheffield, Sheffield S3 7RH, UK*
[3]*Astrophysics Research Institute, Liverpool John Moores University, Liverpool L3 5RF, UK*
[4]*ARC, School of Mathematics and Physics, Queen's University Belfast, University Road, Belfast BT7 1NN, UK*
[5]*Instituto de Astrofísica de Canarias, Vía Láctea s/n, E-38205 La Laguna, Spain*

ABSTRACT

We have measured the transmission spectrum of the extremely inflated hot Jupiter WASP-52b using simultaneous photometric observations in Sloan Digital Sky Survey u', g' and a filter centred on the sodium doublet (Na I) with the ULTRACAM instrument mounted on the 4.2-m William Herschel Telescope. We find that Rayleigh scattering is not the dominant source of opacity within the planetary atmosphere and find a transmission spectrum more consistent with wavelength-independent opacity such as from clouds. We detect an in-transit anomaly that we attribute to the presence of stellar activity and find that this feature can be more simply modelled as a bright region on the stellar surface akin to solar faculae rather than spots. A spot model requires a significantly larger planet/star radius ratio than that found in previous studies. Our results highlight the precision that can be achieved by ground-based photometry with errors in the scaled planetary radii of less than one atmospheric scale height, comparable to *Hubble Space Telescope* observations.

Key words: stars: individual: WASP-52 – planetary systems – starspots.

1 INTRODUCTION

Transmission spectroscopy using *Hubble Space Telescope* (*HST*)/Space Telescope Imaging Spectrograph (STIS) was used to detect the first spectral feature of any exoplanet, that of the narrow core of atomic sodium originating from the upper atmosphere of HD 209458b (Charbonneau et al. 2002). Broad-band opacity sources were later detected in this planet's atmosphere in the form of the pressure broadened wings of Na I (Sing et al. 2008) and a blueward slope in the transmission spectrum interpreted as Rayleigh scattering by H_2 (Lecavelier Des Etangs et al. 2008b). This feature was also seen in *HST* data for HD 189733b (Pont et al. 2008; Sing et al. 2011b), however the absence of the broad wings of Na I suggested the presence of silicate condensates in the upper atmosphere of the planet (Lecavelier Des Etangs et al. 2008a). Recent studies of hot Jupiters with *HST* have revealed a diverse array of atmospheres from clear to cloudy (e.g. Sing et al. 2016). These studies have included the detections of Rayleigh scattering by high altitude hazes also in WASP-12b (Sing et al. 2013), additional unknown optical absorbers in HAT-P-1b (Nikolov et al. 2014), a cloud deck masking

the majority of the Na I absorption and near-infrared water features in WASP-31b (Sing et al. 2015) and a clear atmosphere consistent with solar and subsolar metallicities in WASP-39b (Fischer et al. 2016; Sing et al. 2016).

Ground-based measurements of hot Jupiter transmission signals have also found success, beginning with the detection of the narrow component of Na I in HD 189733b (Redfield et al. 2008) and HD 209458b (Snellen et al. 2008; Langland-Shula et al. 2009). More recent results have included further detections of sodium (e.g. Wood et al. 2011; Zhou & Bayliss 2012), potassium (e.g. Sing et al. 2011a; Wilson et al. 2015), blueward scattering slopes (e.g. Jordán et al. 2013; Stevenson et al. 2014) and atmospheres dominated by clouds or hazes (e.g. Gibson et al. 2013a; Mallonn & Strassmeier 2016).

Although there has been success with ground-based spectroscopic observations they are more susceptible to systematics arising from, for example, differential slit losses (e.g. Sing et al. 2012). A simpler approach, which avoids this problem, is to use photometers to perform simultaneous broad-band multiwavelength measurements. These studies have included evidence for large blueward slopes (e.g. Southworth et al. 2012, 2015; Mancini et al. 2016a), enhanced absorption around the alkali metal lines (e.g. Mancini et al. 2013; Bento et al. 2014) and transmission spectra most

[*]E-mail: james.kirk@warwick.ac.uk

consistent with clouds (e.g. Mallonn et al. 2015b). By observing the planetary radius at carefully selected wavelengths we can probe for the existence of Rayleigh scattering and the broad absorption wings of the Na I doublet that are expected to be present in the cloud-free atmospheres of hot Jupiters (Seager & Sasselov 2000).

Transmission spectroscopy is often focused on inflated hot Jupiters; planets with very low density due to their large radii and relatively low masses. As a result of their low densities, low surface gravities and high temperatures these planets have large atmospheric scale heights, H, given by

$$H = \frac{kT}{g\mu},\qquad(1)$$

where k is Boltzmann's constant, T is the temperature of the planet, g is the acceleration due to gravity and μ is the mean molecular mass. The outermost $\sim$5 scale heights may account for up to 10 per cent of the cross-sectional area of a hot Jupiter, where different atmospheric species can affect the observed transmission spectrum (Brown 2001). The relative size of the planet's scale height to the stellar disc governs the amplitude of the transmission signal.

WASP-52b (Hébrard et al. 2013) is an extremely inflated hot Jupiter, with a mass of 0.46 M_J and radius of 1.27 R_J giving it a mean density of 0.299 g cm^{-3}. It orbits its 0.87 $M_\odot$ K2V host star with a period of 1.75 d. Because of the combination of the inflated planetary radius with the small radius of the host (0.79 R$_\odot$), it shows a deep transit in the WASP photometry (2.7 per cent). From the table of system parameters (Table 2; Hébrard et al. 2013), and assuming a Jupiter mean molecular mass of 2.3 times the mass of a proton, the scale height of WASP-52b is calculated to be 731 km. This makes WASP-52b an exceptional target for transmission spectroscopy as the difference in the transit depth corresponding to one atmospheric scale height is 4.4×10^{-4}, at least three times stronger than that of HD 189733b.

In this paper we present multiwavelength observations of WASP-52b taken using the high speed multiband photometer ULTRACAM (Dhillon et al. 2007).

2 OBSERVATIONS

WASP-52b was observed on the night of the 2012 September 7 using the ULTRACAM (Dhillon et al. 2007) instrument on the 4.2-m William Herschel Telescope (WHT), La Palma. ULTRACAM is a high speed triple beam CCD photometer. Incoming light is split into three bandpasses, using two dichroics, and re-imaged on to three CCDs at a resolution of 0.3 arcsec pixel^{-1}, with a field of view of 5 arcmin.

ULTRACAM is particularly useful for the ground-based application of transmission spectroscopy as it simultaneously takes measurements at three different wavelengths, enabling the transit depth to be measured as a function of wavelength (e.g. Copperwheat et al. 2013; Bento et al. 2014). The use of frame transfer CCDs allow for high frame rates (up to 300 Hz) with little dead time (24 ms), which is useful to avoid saturation when observing bright stars and enables many more sky flats to be taken.

The observations were made using Sloan Digital Sky Survey (SDSS) u' [$\lambda_{central} = 3557$ Å, full width at half-maximum (FWHM) = 599 Å] and g' ($\lambda_{central} = 4825$ Å, FWHM = 1379 Å) filters and a filter centred on the Na I doublet ($\lambda_{central} = 5912$ Å, FWHM = 312 Å). These filters were selected to probe for Rayleigh scattering by observing the difference in transit depth between the u' and g' bands and to search for the broad wings of the sodium doublet with the Na I filter.

The observations were performed with moderate telescope defocusing ($\sim$3 arcsec) in windowed mode with exposure times of 0.76 s in the red and green channels and a cadence of 0.79 s. Because of the reduced photon count in the blue channel multiples of 10 frames were averaged on-chip before readout, leading to a 7.9 s exposure time in this channel.

The moon was at 54 per cent illumination on the night of our observations and we analysed the data with an airmass varying from 1.41 → 1.06 → 2.00.

All the data were reduced using the ULTRACAM data reduction pipeline[1] with bias subtraction and flat-fielding performed in the standard way. Aperture photometry was performed for all frames using a fixed aperture. Initially, many reductions were performed with a variety of aperture sizes and the signal-to-noise ratio was calculated for each using the ratio of aperture counts to aperture errors. The optimal aperture radius was found to be 18 pixels with a sky annulus of inner radius 23 pixels and outer radius 27 pixels.

Some of the observations of WASP-52 were taken through cloud, seen as dips in transmission in the raw light curves, which had to be removed before analysis. These were well defined, discrete events, with good quality data taken between the clouds. The cloudy data were removed using an iterative process. An array of running medians was calculated over a sliding box of 600 data points in the red and green arms and 60 points in the blue. This array of running medians was then subtracted from the raw data to flatten it. The median absolute deviation (MAD) of this subtracted array was calculated and σ clipping performed to remove those data points lying at $\geq$6σ from the MAD. This process was then repeated with a smaller sliding box of 400 data points in the red and green and 40 in the blue with a final σ cut at 5σ from the MAD. The σ clipping was performed on both the target and comparison star independently and only those frames that passed the sigma cut for both were kept, resulting in the removal of 20 per cent of the data. After the σ clipping and binning of the red and green channels to the cadence of the blue channel, there were 2494 data points in each of the three light curves at a cadence of 7.9 s giving us excellent sampling even after the cleaning of the data.

Differential photometry was subsequently performed to remove the worst effects of telluric extinction using a comparison star with similar magnitude and colour to WASP-52 (BD+08 5023, 23:14:12.026, +08:50:56.28). This star has a V magnitude of 10.59 and $B - V$ colour of 0.86, whilst WASP-52 has a V magnitude of 12.22 and $B - V$ colour of 0.82. The comparison star was checked and found to be photometrically stable. Combinations of fainter stars in the field were tested as comparison stars but led to more scatter in the differential light curve than division by the single, bright comparison.

3 DATA ANALYSIS

3.1 Light-curve fitting with analytic model

We initially fitted the differential light curves with analytic limb-darkened transit light curves (Mandel & Agol 2002) using a Markov chain Monte Carlo (MCMC) algorithm, implemented through the EMCEE (Foreman-Mackey et al. 2013) PYTHON package. A quadratic limb darkening law was used and fit simultaneously with a long time-scale trend so as not to bias the derived radii. In the red and

[1] http://deneb.astro.warwick.ac.uk/phsaap/software/ultracam/html/index.html
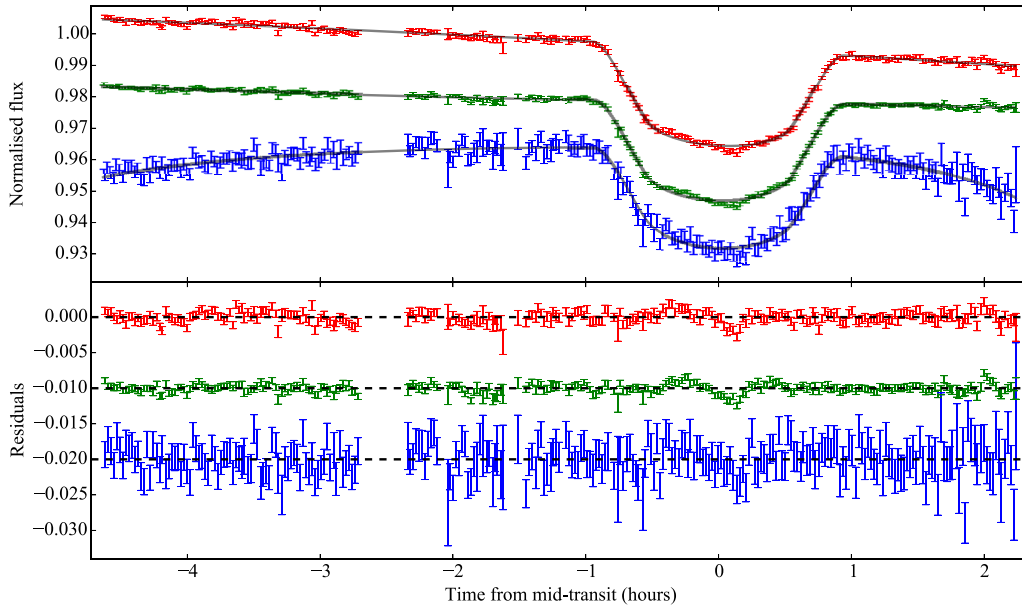
Figure 1. MCMC fits of analytic quadratic limb-darkened transit light curves (Mandel & Agol 2002) revealing the presence of an in-transit anomaly. The upper panel shows the fits to each of the three wavelengths; Na I (top), g' (middle) and u' (bottom) with the latter two light curves each offset by -0.02 for clarity. The lower panel shows the residuals from these fits with the latter two offset by -0.01 and -0.02, respectively.

green channels, this trend was fit with a second-order polynomial whilst in the blue it was fit as a function of airmass since it was clearly related to extinction. In order to fit the airmass term in the blue channel, an extinction coefficient that varied quadratically in time was used, which replicated the trend well. An extinction coefficient that varied linearly in time was also tested but could not fit the sharp downturn in the blue light curve at the end of the night (Fig. 1).

The scaled semimajor axis, a/R_*, inclination of the orbit and the time of mid transit, T_0, were tied across the three light curves when fitting. The parameters that were fit individually in each of the channels were the ratio of planet to star radius R_P/R_*, the second limb darkening coefficient $u2$ and the parameters defining the long time-scale trend. The first limb darkening coefficient, $u1$, was held fixed in the fitting as there is a degeneracy between the limb darkening parameters which can affect the light-curve solution (Southworth 2008). The limb darkening coefficients and priors were chosen from the tables of Claret & Bloemen (2011). Uniform priors were adopted for all the model parameters, with the MCMC walkers started at the values from Hébrard et al. (2013).

The resulting fits of the analytic limb-darkened transit light curves are shown in Fig. 1. The strongest residual across the whole light curve in all three wavelengths is seen during transit and is consistent across the three bands. This residual is akin to the planet occulting areas of stellar activity. We considered the possibility that this anomaly could have been associated with the use of incorrect limb darkening coefficients but no choice of coefficients could replicate this feature.

3.2 Fitting of star spot model

The presence of the in-transit anomaly after the fitting of limb-darkened analytic light curves motivated the use of spot models. Star spot occultations have been seen in the transit light curves of several planets, including HD 189733b (Pont et al. 2007; Sing et al. 2011b), TrES-1b (Dittmann et al. 2009; Rabus et al. 2009),

CoRoT-2b (Huber et al. 2009; Wolter et al. 2009; Silva-Valio et al. 2010), HAT-P-11b (Deming et al. 2011; Sanchis-Ojeda & Winn 2011; Béky et al. 2014a), WASP-4b (Sanchis-Ojeda et al. 2011; Hoyer et al. 2013), WASP-19b (Huitson et al. 2013; Mancini et al. 2013; Mandell et al. 2013; Tregloan-Reed, Southworth & Tappert 2013; Sedaghati et al. 2015), HATS-2b (Mohler-Fischer et al. 2013), Kepler-63b (Sanchis-Ojeda et al. 2013), Qatar-2b (Mancini et al. 2014) and HAT-P-36b (Mancini et al. 2015).

If a planet occults a spot (a region cooler than the surrounding photosphere) it blocks less of the stellar flux than compared with its transit across the hotter pristine stellar disc. This results in a bump during transit and therefore a smaller derived planetary radius. Star spot activity is not unexpected for WASP-52 since Hébrard et al. (2013) found modulations in its light curve and chromospheric emission peaks in the Ca II H+K lines. Using these modulations they calculated the rotation period of WASP-52 to be 16.4 d.

Spot crossing events have been modelled with a variety of techniques, such as PRISM (Tregloan-Reed et al. 2013), SOAP-T (Oshagh et al. 2013) and SPOTROD (Béky, Kipping & Holman 2014b). For this analysis we used SPOTROD to generate the spot affected light curves and wrote an MCMC wrapper around these generated light curves to fit them simultaneously across the bands and with the same long time-scale trends as before. We chose to use SPOTROD due to the speed of its integration, which uses polar coordinates in the projection plane. The integration with respect to the polar coordinate is done analytically so that only the integration with respect to the radial coordinate needs to be performed numerically. To calculate the projection of the planet on the stellar surface, SPOTROD calculates the arrays of planar orbital elements ξ and η, using the formalism of Pál (2009), and assumes the same limb darkening law for the spot as for the star.

The system parameters were again fit across the three light curves simultaneously (although this time fitting for impact parameter, b, rather than the inclination, as required by SPOTROD) and with the addition of the parameters defining the spots. The fitting of one spot was tested but was unable to fit both bumps on either side of the

transit mid-point, therefore two spots were used in further analysis. The parameters defining each spot were the longitude, latitude, radius ratio of spot to star and ratio of the spot flux to stellar flux (with 1 being a spot with the same flux as the pristine photosphere and 0 being a spot with zero flux). We held $u1$ fixed as before but now also put Gaussian priors on $u2$ with means equal to the values from Claret & Bloemen (2011) and standard deviations from the propagated errors in the effective temperature and surface gravity of the host star. This prior was necessary as the limb darkening and spot models can play off each other in trying to fit the transit shape.

The MCMC was initiated with the system parameters equal to those in Hébrard et al. (2013) and was run for 10 000 steps in burn in and another 10 000 steps in the production run. There were 31 fitted parameters with 124 walkers. The parameters governing a spot's characteristics are correlated with one another. The correlation between spot contrast and size has been shown previously by e.g. Pont et al. (2007), Wolter et al. (2009), Tregloan-Reed et al. (2013) and Béky et al. (2014b). We initiated the MCMC starting positions with spots at various, randomly selected, latitudes on the stellar surface so as not to bias the fits and test for convergence. After the burn in phase the error bars in the data points were rescaled to give a reduced χ^2 of unity.

After the first MCMC chain, a second MCMC was run but this time with the parameters that were tied across channels fixed to the results from the first run (a/R_*, b, T_0 and the spot sizes and positions). Correlations with these parameters cause R_P/R_* to move up and down together across the three wavelengths, contributing to the uncertainty in the absolute planetary radius in each of the bands. Since we are concerned with the shape of the transmission spectrum, we are interested in the relative radii between the bands and not the absolute planetary radius, thus motivating the second run of the MCMC with fixed system parameters.

We present the best-fitting spot model in Fig. 2, after the second MCMC run, with the results in Table 1 and transmission spectrum in Fig. 6 (blue squares).

With the sizes and contrasts calculated from SPOTROD, we were able to create a schematic of the stellar surface (Fig. 3, left-hand panel) and consider what filling factor would reproduce the derived contrasts (Section 4.1.1 and Fig. 3, right-hand panel). This figure displays the large regions of stellar activity along the transit chord. The second spot crossing event composed of a smaller region of higher contrast (0.2 in the g' band, Table 1). The error in the contrast of this dark spot also allowed for a larger, less dark spot.
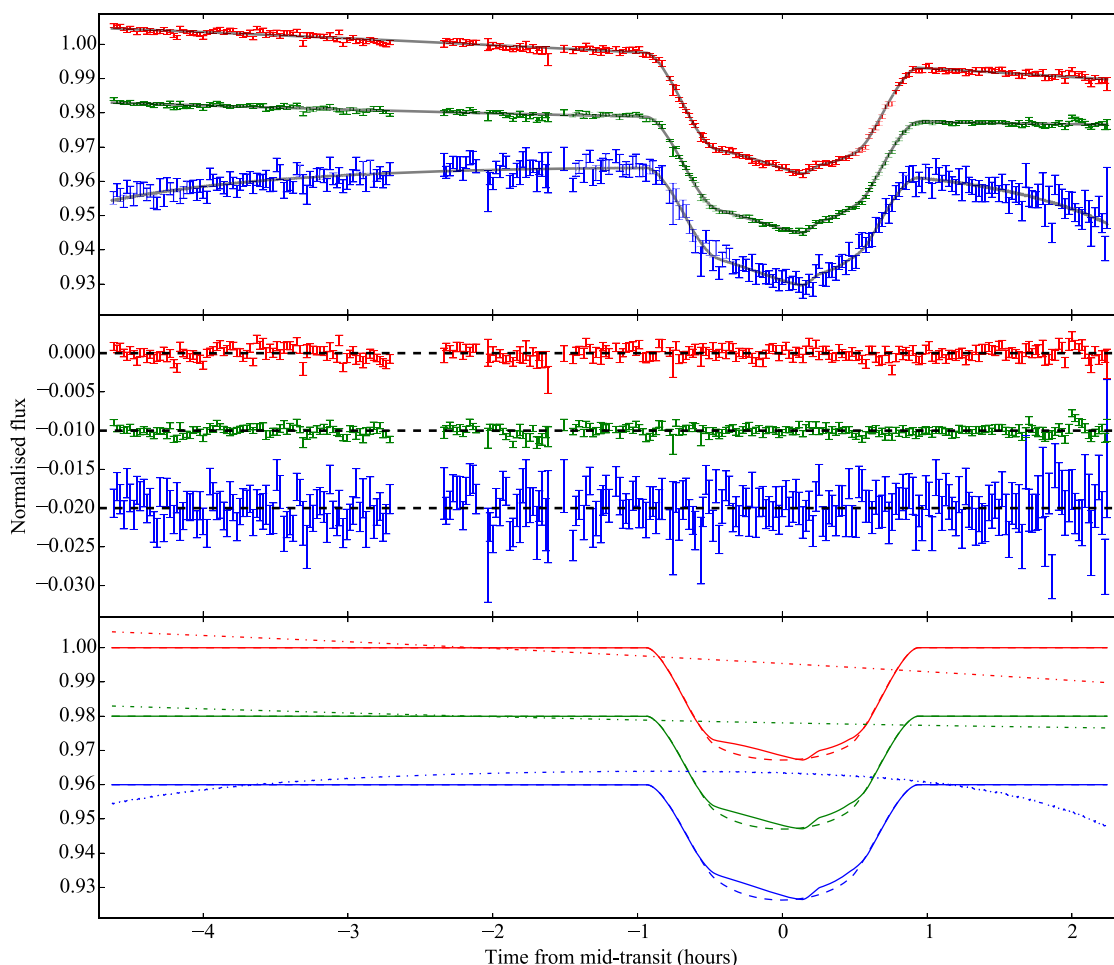
Figure 2. MCMC fit of spot model with the occultation of two areas of stellar activity at temperatures lower than the pristine photosphere. The top panel shows the best-fitting model for each of the three wavelengths from Na I (top), g' (middle) and u' (bottom), offset by -0.02 and -0.04. The middle panel shows the residuals from these fits, offset by -0.01 and -0.02, whilst the bottom panel shows the constituents of each model, offset by -0.02 and -0.04. The solid line shows the best-fitting spot model with the dashed line representing how the model would appear in the absence of spots. The dot–dashed line shows the long time-scale term fitted by a second-order polynomial in each of the Na I and g' bands and by a function of airmass in the u' band.

Table 1. Results from fitting the transit light curves with both spots and faculae to model the stellar activity. Note: x position of the spots can take values between ± 1 which are analogous to longitudes of $\pm 90°$ whilst y position takes values between 1 and 0 corresponding to latitudes of $\pm 90°$. Spot contrast is defined as the ratio of spot flux to stellar flux so a value of unity gives a spot of equal brightness to the surrounding photosphere.

Parameter	Symbol	u'	g'	Na I
Two-spot model				
Time of mid-transit (MJD)[a]	T_0	–	56178.12742 ± 0.00005	–
Scaled semimajor axis[a]	a/R_*	–	6.99 ± 0.04	–
Impact parameter[a]	b	–	$0.656^{+0.006}_{-0.007}$	–
Radius ratio	R_P/R_*	$0.1759^{+0.0005}_{-0.0004}$	0.1751 ± 0.0004	0.1757 ± 0.0008
Limb darkening coeff.[b]	u_1	0.643	0.529	0.381
Limb darkening coeff.	u_2	0.169 ± 0.008	0.233 ± 0.008	$0.290^{+0.009}_{-0.010}$
Spot 1 x position[a]	x_1	–	-0.19 ± 0.03	–
Spot 1 y position[a]	y_1	–	$0.91^{+0.03}_{-0.04}$	–
Spot 1 radius ratio[a]	r_1/R_*	–	$0.36^{+0.04}_{-0.03}$	–
Spot 1 contrast	ρ_1	0.61 ± 0.02	0.66 ± 0.02	0.63 ± 0.04
Spot 2 x position[a]	x_2	–	$0.38^{+0.02}_{-0.007}$	–
Spot 2 y position[a]	y_2	–	$0.69^{+0.02}_{-0.03}$	–
Spot 2 radius ratio[a]	r_2/R_*	–	$0.07^{+0.08}_{-0.006}$	–
Spot 2 contrast	ρ_2	0.17 ± 0.07	0.19 ± 0.07	0.3 ± 0.1
Facula model				
Time of mid-transit (MJD)[a]	T_0	–	56178.12740 ± 0.00004	–
Scaled semimajor axis[a]	a/R_*	–	7.23 ± 0.05	–
Impact parameter[a]	b	–	$0.593^{+0.008}_{-0.009}$	–
Radius ratio	R_P/R_*	0.1632 ± 0.0003	0.1641 ± 0.0003	0.1657 ± 0.0006
Limb darkening coeff.[b]	u_1	0.643	0.529	0.381
Limb darkening coeff.	u_2	0.161 ± 0.009	0.239 ± 0.009	0.29 ± 0.01
Facula x position[a]	x_1	–	$0.123^{+0.007}_{-0.008}$	–
Facula y position[a]	y_1	–	0.62 ± 0.03	–
Facula radius ratio[a]	r/R_*	–	$0.20^{+0.01}_{-0.02}$	–
Facula contrast	ρ	1.119 ± 0.007	1.089 ± 0.008	1.08 ± 0.01

Notes. [a]Parameter is shared and fit across channels with the result quoted in the g' column only and is held fixed at the value for the second MCMC run. The errors on all other parameters are those after the second MCMC run.
[b]Parameter not fit by model.

3.3 Fitting of bright region model

As an alternative interpretation, the in-transit anomaly was also modelled as a bright feature analogous to solar faculae. Solar faculae are bright regions on the solar photosphere which display limb brightening behaviour (e.g. Unruh, Solanki & Fligge 1999). They are often cospatial with sunspots but not perfectly so (e.g. Haywood et al. 2016).

The effects of occultations of bright regions in exoplanet transits have been discussed by Oshagh et al. (2014) and could lead to an observable anomaly in transit data. There has not yet been any conclusive evidence of a facula occultation in a transit light curve although Mohler-Fischer et al. (2013) found evidence for a hotspot in GROND photometry of HATS-2b. They detected a bright feature in the Sloan g band, which covered the Ca II lines, that was consistent with a chromospheric plage occultation.

SPOTROD was also used to model the facula scenario but instead of two individual spots with flux ratios <1, a single feature was modelled with a flux ratio of >1. This fitting method produced the fits seen in Fig. 4 with the results in Table 1. This model was able to reproduce the in-transit anomaly with an equally good fit as the two-spot model but with six fewer parameters. The transmission spectrum resulting from the facula model is also shown in Fig. 6 (red triangles). In contrast to the flat transmission spectrum resulting from the fitting of spots, the fitting of a facula led to a slope in the planetary radius increasing towards the red (Fig. 6).

4 DISCUSSION

4.1 Spots or faculae?

It is difficult to distinguish between the spot and facula models of Sections 3.2 and 3.3 using the quality of the fits alone. Application of the Bayesian information criterion (BIC; given by BIC $= \chi^2 + k \ln N$ with k free parameters and N data points) favours the facula model because of the similar χ^2 and six fewer free parameters, with a value of >10 lower than that of the spot model. However, our prior knowledge of transit light curves tends to favour the spot model because spots are more commonly detected (e.g. e.g. Pont et al. 2007; Sing et al. 2011b; Mancini et al. 2013; Tregloan-Reed
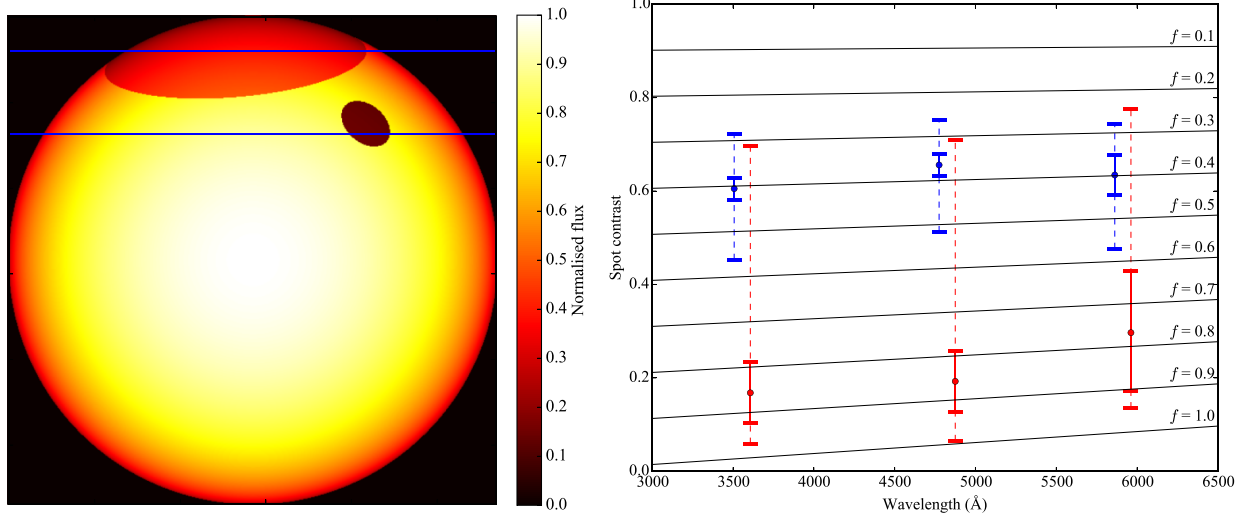
Figure 3. Left-hand panel: schematic illustration of how the stellar surface may appear with the active regions derived from the fitting of the spot model and contrasts consistent with those in the g' band. The blue lines indicate the planet's transit chord. Right-hand panel: plot of the derived spot contrasts for both spot #1 (blue) and spot #2 (red) in each of the three wavelengths, offset in the *x*-axis by -50 and $+50$ Å, respectively, for clarity. The dashed error bars show the error in the absolute spot contrasts whilst the solid error bars give the relative uncertainties between the bands for our best-fitting system parameters. Overplotted are the calculated contrasts for a spot with $\Delta T = 1500$ K (consistent with predictions for K stars) with varying filling factors f (solid black lines).
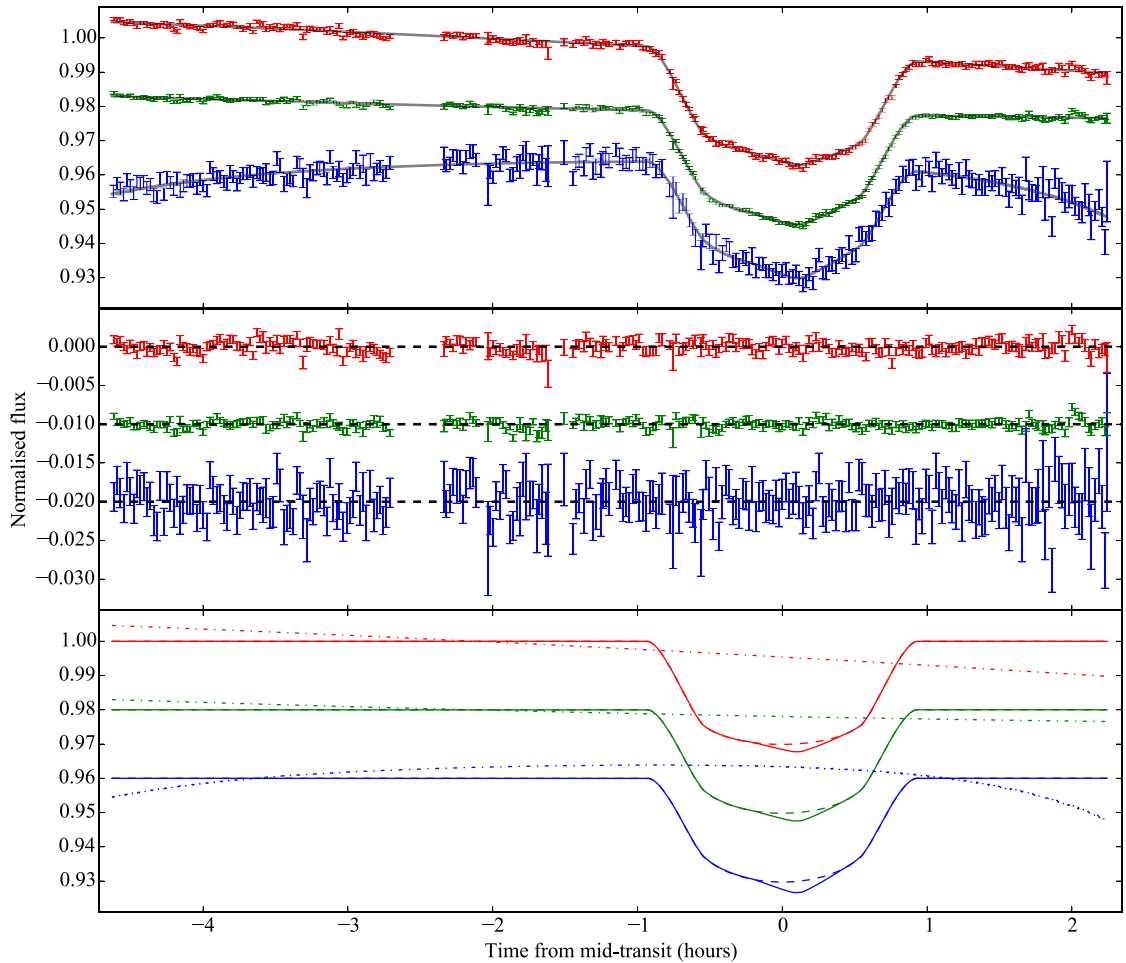
Figure 4. The same representation as in Fig. 2 but this time showing the result of the fitting of a bright spot, analogous to a facula, occulted on the stellar surface. This bright spot leads to a dip in the in-transit data (bottom panel, solid lines) as compared to a transit free of such spots (bottom panel, dashed line).

et al. [2013]) than faculae or bright regions (e.g. Mohler-Fischer et al. [2013]).

A second approach to distinguishing between these models is to compare our fitted planet radius with that from independent studies. It can be seen in the model light curves of Figs [2] and [4] that our spot and facula models imply different underlying depths of transit. In the spot model the anomaly is treated as two bumps (bottom panel of Fig. [2]), and so the underlying transit is deeper than in the facula model, where the anomaly is treated as a single dip (Fig. [4]). This difference can be seen in our fitted planet/star radius ratios (Table [1]) where the spot model implies a planet radius that is 15σ larger than the value from the facula model. The planet/star radius ratio has been previously measured by Hébrard et al. ([2013]) using six individual transits, and found to be 0.1646 ± 0.0012. This is consistent with our value from the facula model (within 1σ), and inconsistent with our value from the spot model ($>6\sigma$ discrepancy).

While this paper was under review, another study of WASP-52b was published on arXiv (Mancini et al. [2016b]) including a further eight transits. Spots were clearly detected in five of these light curves and the system parameters measured accounted for these spots. Again, we find that the planet/star radius ratio is consistent with a facula model (within 1σ) and inconsistent with our spot model (12σ discrepancy).

We also consider the possibility that unocculted spots could be the cause of the discrepant $R_{\rm P}/R_*$ values we derive from the spot model but find this would require a total dimming of the star of 12 per cent, which we consider unlikely. This is discussed in more detail in Section 4.3.

We conclude that the comparison of our planet/star radius ratios with independent studies strongly favours the presence of a facula in our observed transit. Nevertheless, in Sections 4.1.1 and 4.1.2 we discuss the implications of both models.

4.1.1 Spot properties

The best-fitting spot model indicates two large regions of stellar activity (Fig. [3], left-hand panel) which are consistent with the majority of the in-transit data being activity affected (Fig. [2]).

Although spot modelling codes, including SPOTROD, fit spots as circular areas on the stellar surface, in reality these may be areas of several small spots which may be arranged in more complex configurations on the stellar surface. If the features in our light curves really were single spots with temperatures consistent with those expected for K stars, we would expect to see large amplitude bumps and a strong colour dependence. When considering the spots resulting from our modelling however, we believe that the spots are more accurately interpreted as active regions, with spots and pristine photosphere contained within, instead of two large individual spots (Fig. [3]).

When considering these complexes of smaller starspots, it is useful to consider the area ratio of spots to uncontaminated photosphere within each of these regions, which we define here as the filling factor, f. This quantity can be related to the spot's contrast, ρ, through

$$\rho = \frac{f F_\bullet(\lambda) + (1-f) F_*(\lambda)}{F_*(\lambda)}, \tag{2}$$

where $F_\bullet$ is the flux of the spot and F_* is the flux of the star.

Berdyugina ([2005]) plotted the observed temperature differences of spots for several different stellar effective temperatures. For K stars, the spot temperature differences (ΔT) lie in the region of 1250–1500 K.

Because of the degeneracy between spot size and contrast the spot contrasts have large error bars in Fig. [3] (right-hand panel). However, by fixing the spot sizes and positions at the best-fitting values from the first MCMC run, the second run gave the relative uncertainty in the spot contrasts across the bands rather than the absolute uncertainty, as with the planetary radii. When considering the relative spot contrasts (Fig. [3], right-hand panel, solid error bars) it can be seen that the contrasts and colour dependence of these active regions are consistent with a ΔT of 1500 K, given a single filling factor f.

For the smaller spot (Fig. [3], right-hand panel, red error bars) we infer a higher filling factor (approximately 0.85), and for the larger spot (Fig. [3], right-hand panel, blue error bars) a lower filling factor (approximately 0.4). The larger spot can be understood as a large active region on the stellar surface with a relatively low density of smaller dark spots. The smaller spot however has a high density of smaller dark spots leading to the greater contrast.

4.1.2 Facula properties

As discussed in Section 4.1 the occultation of a bright region, analogous to a solar facula, is our favoured interpretation for these data. Unlike spots, the flux contrasts of faculae increase at the stellar limb as they display limb brightening behaviour (Unruh et al. [1999]) and so the assumption that the modelled spots follow the same limb darkening as the star does not hold in this case. Therefore equation (2) cannot be used to calculate the temperature of the facula so we report only the flux contrasts of the facula in Table [1] which indicate the hotspot is $\sim$10 per cent brighter in all three bands. Solar faculae are also able to display such contrasts however, at the solar limb with a high viewing angle (e.g. Unruh et al. [1999]; Ahern & Chapman [2000]). At the viewing angle of our facula, we would only expect to see a $\sim$3 per cent contrast if this were a solar facula (e.g. Ahern & Chapman [2000]). However, since WASP-52 is a more active and later-type star it is possible it could display higher contrast faculae.

4.2 Measuring the residual red noise

In order to measure the systematic red noise in the residuals, we observed how the fractional root mean square (rms) of the residuals with respect to the flux varied with binning of the data. Fig. [5] shows the rms for a number of different bin sizes. The line overlaid corresponds to pure, Gaussian, white noise with a gradient equal to $1/\sqrt{N}$, where N is the number of points per bin. The factor β quantifies how the actual binning gradient deviates from pure white noise (Winn et al. [2008]). The β factors found here show that the residuals do deviate from pure white noise but with amplitudes of only 0.5 mmag.

4.3 Unocculted spots

Just as the effects of occulted spots or bright regions must be taken into account when calculating the planetary radius, so must the effects of those regions which are not seen in the transit. As the photometric modulation of Sun-like stars with high magnetic activity is dominated by dark spots (e.g. Shapiro et al. [2014]), we only consider the effect of unocculted spots on our derived transit depths. Unocculted spots cause the observed stellar flux to decrease, increasing the transit depth as compared to a spot-free surface. This effect needs to be taken into account with a wavelength-dependent depth correction.
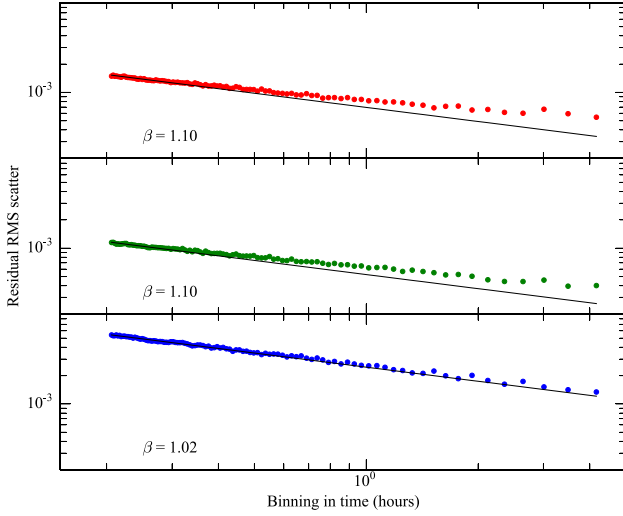
Figure 5. The residual rms scatter once the spot model has been subtracted for Na I (top panel), g' (middle panel) and u' (bottom panel). The error bars on the data points were rescaled to give a $\chi_\nu^2 = 1$. β quantifies how the measured noise deviates from pure Gaussian white noise (solid black lines).

Following the formalism of Sing et al. (2011b), the variation in transit depth, $\Delta d/d$, can be related to the fractional decrease of the stellar flux due to unoccluded spots at a reference wavelength λ_0, $\Delta f(\lambda_0, t)$, the flux of the pristine stellar disc, $F_\lambda^{T_{\text{star}}}$, and the flux of

the spot, $F_\lambda^{T_{\text{spot}}}$, through

$$\frac{\Delta d}{d} = \Delta f(\lambda_0, t)\left(1 - \frac{F_\lambda^{T_{\text{spot}}}}{F_\lambda^{T_{\text{star}}}}\right) \Bigg/ \left(1 - \frac{F_{\lambda_0}^{T_{\text{spot}}}}{F_{\lambda_0}^{T_{\text{star}}}}\right) \qquad (3)$$

leading to a variation in the ratio of planet radius to stellar radius of

$$\Delta(R_{\text{p}}/R_{\text{star}}) \approx \frac{1}{2}\frac{\Delta d}{d}(R_{\text{p}}/R_{\text{star}}). \qquad (4)$$

We used stellar atmosphere models (ATLAS9; Kurucz 1993) to generate synthetic spectra of the star and a spot with the maximum temperature contrast of 1500 K cooler than the surrounding photosphere (Berdyugina 2005).

If we rearrange the above equations for $\Delta f(\lambda_0, t)$, we can estimate the percentage of total dimming required to bring our derived R_{P}/R_* values into agreement with those of Hébrard et al. (2013). We find that the total dimming must be >12 per cent at a reference wavelength of 6000 Å, considerably higher than the 1 per cent amplitude measured by Hébrard et al. (2013). As a result of this, we do not believe that unoccluded spots are the cause of the discrepancy in the R_{P}/R_* values resulting from the spot model.

To calculate what effect unoccluded spots have on the shape of our transmission spectra, we used a total dimming of 1 per cent at a reference wavelength of 6000 Å to calculate $\Delta(R_{\text{P}}/R_*)$ in each of our three light curves. The difference in $\Delta(R_{\text{P}}/R_*)$ between the red and the blue light curves is 10 times smaller than the 1σ error bars and so unoccluded spots do not affect the shape of our transmission spectrum (Fig. 6) or the conclusions we draw from it.
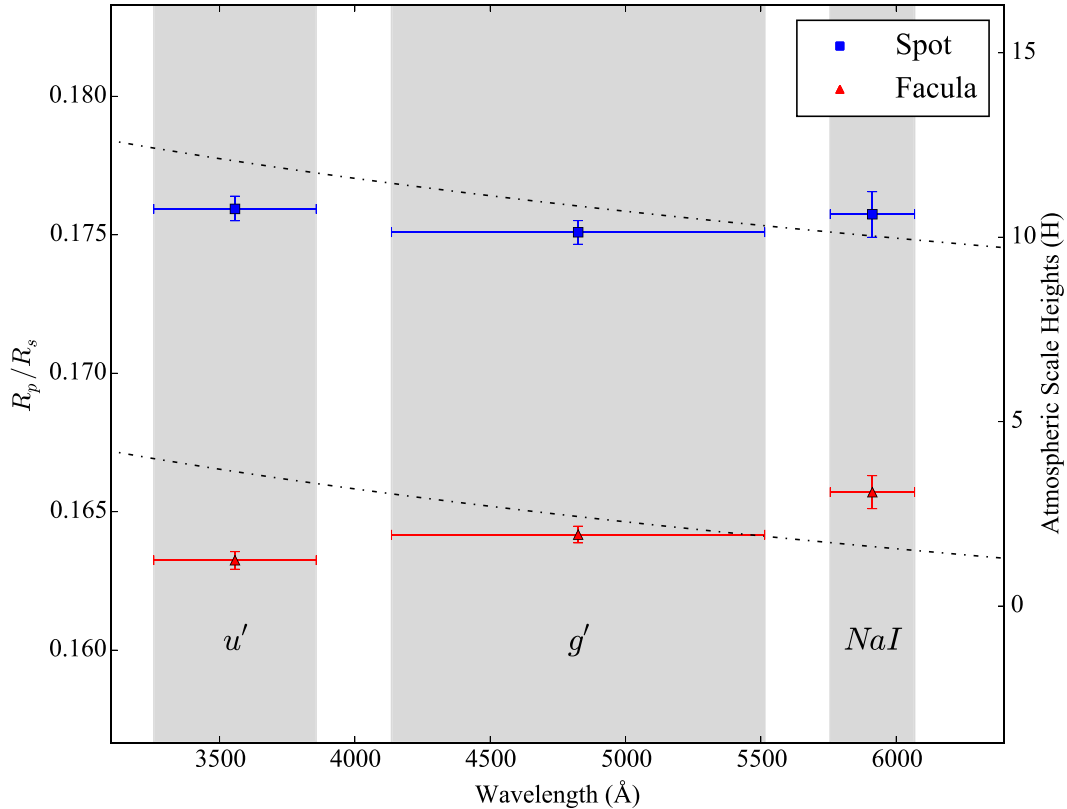
Figure 6. Transmission spectrum of WASP-52b. The errors in the *x*-axis are quoted as the FWHM of the filters used; u', g' and Na I. The results from both the spot (blue squares) and facula (red triangles) models are included. Overplotted is a Rayleigh scattering slope (black dot–dashed line) which is ruled out with >3σ significance. The scale height axis is calculated using the value for WASP-52b's surface gravity from Hébrard et al. (2013).

Table 2. Comparison between derived system parameters from this work with WASP-52b's discovery paper (Hébrard et al. 2013).

Parameter (units)	Symbol	This work (spots)	This work (facula)	Hébrard et al. (2013)
Orbital period (d)	P	–	–	1.7497798 ± 0.0000012
Semi major axis (au)	a	–	–	0.0272 ± 0.0003
Orbital eccentricity	e	–	–	>0 (fixed)
Planetary equilibrium temperature (K)	T_P	–	–	1315 ± 35
Transit epoch (HJD – 245 0000.0) (d)[a]	T_0	6178.62742 ± 0.00005	6178.62740 ± 0.00004	5793.68143 ± 0.00009
Scaled stellar radius[a]	R_*/a	0.1431 ± 0.0009	0.1383 ± 0.0008	0.1355 ± 0.0020
Impact parameter (R_*)[a]	b	$0.656^{+0.006}_{-0.007}$	$>0.593^{+0.008}_{-0.009}$	0.60 ± 0.02
Orbital inclination (°)[a]	i	84.62 ± 0.07	85.30 ± 0.08	85.35 ± 0.20
Transit duration (d)[b]	t_T	0.0777 ± 0.0006	0.0772 ± 0.0006	0.0754 ± 0.0005
Planet/star area ratio[b]	$(R_p/R_*)^2$	0.0306 ± 0.0005	0.0270 ± 0.0002	0.0271 ± 0.0004
Stellar density ($\rho_\odot$)[b]	ρ_*	1.50 ± 0.03	1.66 ± 0.03	1.76 ± 0.08
Stellar radius (R$_\odot$)	R_*	–	–	0.79 ± 0.02
Planet radius (R_J)[c]	R_p	1.34 ± 0.04	1.26 ± 0.03	1.27 ± 0.03
Stellar reflex velocity (km s^{-1})	K_1	–	–	0.0843 ± 0.0030
Planet surface gravity (cgs)	$\log g_p$	2.75 ± 0.02	2.83 ± 0.02	2.81 ± 0.03
Planet density (ρ_J)[c]	ρ_p	0.383 ± 0.024	0.204 ± 0.009	0.22 ± 0.02
Planet mass (M_J)[c]	M_p	0.38 ± 0.02	0.41 ± 0.03	0.46 ± 0.02

Notes. [a]Fitted parameter.
[b]Derived from the transit light curve alone.
[c]Derived using stellar radius from Hébrard et al. (2013).

4.4 Transmission spectrum

Fig. 6 displays the derived transmission spectrum for WASP-52b. On this plot are the results from modelling the in-transit anomaly both as spots and as a single facula. The errors in the transmission spectra are those after fitting with the wavelength-independent parameters held fixed at the best-fitting values from the first MCMC run (b, a/R_*, T_0, spot/facula sizes and positions). This resulted in errors of less than one planetary atmospheric scale height.

In the presence of Rayleigh scattering, the expected slope of the planetary radius as a function of wavelength is given by (Lecavelier Des Etangs et al. 2008a)

$$\frac{\mathrm{d}R_p}{\mathrm{d}\ln\lambda} = \frac{k}{\mu g}\alpha T, \qquad (5)$$

where μ is the mean molecular mass of an atmospheric particle taken to be 2.3 times the mass of a proton, k is the Boltzmann constant, g is the planet's surface gravity, $\alpha = -4$ as expected for Rayleigh scattering and T we take as the equilibrium temperature.

Using our derived values for the planet's surface gravity (Table 2) we are able to rule out Rayleigh scattering in this atmosphere with $>3\sigma$ confidence (Fig. 6). The spot model gives a χ^2 of 14.52 for Rayleigh scattering and 2.00 for a flat line, each with 2 degrees of freedom. Therefore the spot model strongly favours a flat transmission spectrum. For the case of the facula model, the transmission spectrum shows an increase in planetary radius towards the red which is not well fit by either a flat line or Rayleigh scattering. The implied increased radius in the red could indicate the detection of the broad wings of Na I.

An absence of Rayleigh scattering has been seen in a handful of planets to date, such as HAT-P-32b (Gibson et al. 2013b), WASP-29b (Gibson et al. 2013a) and HAT-P-19b (Mallonn et al. 2015a). The absence of Rayleigh scattering and any broad spectral features has been attributed to clouds in the upper atmosphere of the planet obscuring any such features. It could be that clouds are masking the spectral features of WASP-52b also.

4.5 Updated system parameters

As outlined in Section 4.1, we compared our results to those of Hébrard et al. (2013) (Table 2). We note that Baluev et al. (2015) also studied WASP-52b in looking for transit timing variations but the results of the parameters that they fit for, R_P/R_* and b, are within the 1σ errors of Hébrard et al. (2013).

All the parameters in Table 2 marked with [b] were derived from the g'-band transit light curve alone, following the prescription of Seager & Mallén-Ornelas (2003). The planet surface gravity was calculated using the equation from Southworth, Wheatley & Sams (2007) which can be derived from the transit light curve but with the addition of the stellar reflex velocity for which we use the value from Hébrard et al. (2013). The parameters that we have held fixed in our fitting (semimajor axis and period) and those which we do not derive are left blank in Table 2. The parameters marked with [c] were derived assuming a stellar radius equal to that of Hébrard et al. (2013).

As discussed in Section 4.1, the differing implied transit depths of the spot and facula models result in significantly different system parameters (Table 2). When modelled as two spots, we find a transit depth $>3\sigma$ larger than that of Hébrard et al. (2013), whereas the facula model results in a transit depth consistent with that of Hébrard et al. (2013).

5 CONCLUSIONS

In this paper we have measured the optical transmission spectrum of the highly inflated hot Jupiter WASP-52b.

Our multiwavelength light curves, observed with WHT/ULTRACAM, have demonstrated that 0.5 mmag precision can be achieved with high-quality ground-based photometry. This leads to errors in our planetary radii of less than one planetary atmospheric scale height, comparable to recent *HST* observations (e.g. Nikolov et al. 2014; Sing et al. 2015; Fischer et al. 2016).

Our transit light curves revealed the presence of regions of stellar activity whose in-transit anomalies were modelled using SPOTROD (Béky et al. 2014b). Although modelled as discrete events, it is likely that the planet in fact transits across latitudes of high stellar activity which may be near continuous across the transit chord.

We find this activity can be most simply modelled as a bright region akin to solar faculae, which results in system parameters consistent with independent studies. The light curves can also be fit with two regions of dark spots but this requires a planet/star radius ratio inconsistent with these studies. As a result, the occultation of a bright region on the host star is the favoured interpretation of the feature seen in the light curves.

We find that Rayleigh scattering is not the dominant source of opacity within the planetary atmosphere. When modelling the in-transit anomalies as spots, we derive a transmission spectrum consistent with wavelength-independent absorption by clouds and find no evidence for any broad sodium absorption although we cannot rule out the presence of the narrow line core. For our favoured facula model, we find an increasing planetary radius towards the red optical which could be interpreted as evidence for the broad wings of Na I.

This work highlights the need for high precision photometry at multiple wavelengths simultaneously to detect and study the effects of stellar activity, in the form of spots and bright regions, on the derived transit parameters.

REFERENCES

Ahern S., Chapman G. A., 2000, Sol. Phys., 191, 71
Baluev R. V. et al., 2015, MNRAS, 450, 3101
Béky B., Holman M. J., Kipping D. M., Noyes R. W., 2014a, ApJ, 788, 1
Béky B., Kipping D. M., Holman M. J., 2014b, MNRAS, 442, 3686
Bento J. et al., 2014, MNRAS, 437, 1511
Berdyugina S. V., 2005, Living Rev. Sol. Phys., 2, 8
Brown T. M., 2001, ApJ, 553, 1006
Charbonneau D., Brown T. M., Noyes R. W., Gilliland R. L., 2002, ApJ, 568, 377
Claret A., Bloemen S., 2011, A&A, 529, A75
Copperwheat C. M. et al., 2013, MNRAS, 434, 661
Deming D. et al., 2011, ApJ, 740, 33
Dhillon V. S. et al., 2007, MNRAS, 378, 825
Dittmann J. A., Close L. M., Green E. M., Fenwick M., 2009, ApJ, 701, 756
Fischer P. D. et al., 2016, ApJ, 827, 19
Foreman-Mackey D., Hogg D. W., Lang D., Goodman J., 2013, PASP, 125, 306
Gibson N. P., Aigrain S., Barstow J. K., Evans T. M., Fletcher L. N., Irwin P. G. J., 2013a, MNRAS, 428, 3680
Gibson N. P., Aigrain S., Barstow J. K., Evans T. M., Fletcher L. N., Irwin P. G. J., 2013b, MNRAS, 436, 2974
Haywood R. D. et al., 2016, MNRAS, 457, 3637
Hébrard G. et al., 2013, A&A, 549, A134
Hoyer S. et al., 2013, MNRAS, 434, 46
Huber K. F., Czesla S., Wolter U., Schmitt J. H. M. M., 2009, A&A, 508, 901
Huitson C. M. et al., 2013, MNRAS, 434, 3252
Jordán A. et al., 2013, ApJ, 778, 184
Kurucz R., 1993, ATLAS9 Stellar Atmosphere Programs and 2 km/s Grid. Kurucz CD-ROM No. 13. Smithsonian Astrophysical Observatory, Cambridge, MA

Langland-Shula L. E., Vogt S. S., Charbonneau D., Butler P., Marcy G., 2009, ApJ, 696, 1355
Lecavelier Des Etangs A., Pont F., Vidal-Madjar A., Sing D., 2008a, A&A, 481, L83
Lecavelier Des Etangs A., Vidal-Madjar A., Désert J.-M., Sing D., 2008b, A&A, 485, 865
Mallonn M., Strassmeier K. G., 2016, A&A, 590, A100
Mallonn M. et al., 2015a, A&A, 580, A60
Mallonn M. et al., 2015b, A&A, 583, A138
Mancini L. et al., 2013, MNRAS, 436, 2
Mancini L. et al., 2014, MNRAS, 443, 2391
Mancini L. et al., 2015, A&A, 579, A136
Mancini L., Kemmer J., Southworth J., Bott K., Mollière P., Ciceri S., Chen G., Henning T., 2016a, MNRAS, 459, 1393
Mancini L. et al., 2016b, preprint (arXiv:e-prints)
Mandel K., Agol E., 2002, ApJ, 580, L171
Mandell A. M., Haynes K., Sinukoff E., Madhusudhan N., Burrows A., Deming D., 2013, ApJ, 779, 128
Mohler-Fischer M. et al., 2013, A&A, 558, A55
Nikolov N. et al., 2014, MNRAS, 437, 46
Oshagh M., Boisse I., Boué G., Montalto M., Santos N. C., Bonfils X., Haghighipour N., 2013, A&A, 549, A35
Oshagh M., Santos N. C., Ehrenreich D., Haghighipour N., Figueira P., Santerne A., Montalto M., 2014, A&A, 568, A99
Pál A., 2009, MNRAS, 396, 1737
Pont F. et al., 2007, A&A, 476, 1347
Pont F., Knutson H., Gilliland R. L., Moutou C., Charbonneau D., 2008, MNRAS, 385, 109
Rabus M. et al., 2009, A&A, 494, 391
Redfield S., Endl M., Cochran W. D., Koesterke L., 2008, ApJ, 673, L87
Sanchis-Ojeda R., Winn J. N., 2011, ApJ, 743, 61
Sanchis-Ojeda R., Winn J. N., Holman M. J., Carter J. A., Osip D. J., Fuentes C. I., 2011, ApJ, 733, 127
Sanchis-Ojeda R. et al., 2013, ApJ, 775, 54
Seager S., Mallén-Ornelas G., 2003, ApJ, 585, 1038
Seager S., Sasselov D. D., 2000, ApJ, 537, 916
Sedaghati E., Boffin H. M. J., Csizmadia S., Gibson N., Kabath P., Mallonn M., Van den Ancker M. E., 2015, A&A, 576, L11
Shapiro A. I., Solanki S. K., Krivova N. A., Schmutz W. K., Ball W. T., Knaack R., Rozanov E. V., Unruh Y. C., 2014, A&A, 569, A38
Silva-Valio A., Lanza A. F., Alonso R., Barge P., 2010, A&A, 510, A25
Sing D. K., Vidal-Madjar A., Désert J.-M., Lecavelier des Etangs A., Ballester G., 2008, ApJ, 686, 658
Sing D. K. et al., 2011a, A&A, 527, A73
Sing D. K. et al., 2011b, MNRAS, 416, 1443
Sing D. K. et al., 2012, MNRAS, 426, 1663
Sing D. K. et al., 2013, MNRAS, 436, 2956
Sing D. K. et al., 2015, MNRAS, 446, 2428
Sing D. K. et al., 2016, Nature, 529, 59
Snellen I. A. G., Albrecht S., de Mooij E. J. W., Le Poole R. S., 2008, A&A, 487, 357
Southworth J., 2008, MNRAS, 386, 1644
Southworth J., Wheatley P. J., Sams G., 2007, MNRAS, 379, L11
Southworth J., Mancini L., Maxted P. F. L., Bruni I., Tregloan-Reed J., Barbieri M., Ruocco N., Wheatley P. J., 2012, MNRAS, 422, 3099
Southworth J. et al., 2015, MNRAS, 447, 711
Stevenson K. B., Bean J. L., Seifahrt A., Désert J.-M., Madhusudhan N., Bergmann M., Kreidberg L., Homeier D., 2014, AJ, 147, 161
Tregloan-Reed J., Southworth J., Tappert C., 2013, MNRAS, 428, 3671
Unruh Y. C., Solanki S. K., Fligge M., 1999, A&A, 345, 635
Wilson P. A. et al., 2015, MNRAS, 450, 192
Winn J. N. et al., 2008, ApJ, 683, 1076
Wolter U., Schmitt J. H. M. M., Huber K. F., Czesla S., Müller H. M., Guenther E. W., Hatzes A. P., 2009, A&A, 504, 561
Wood P. L., Maxted P. F. L., Smalley B., Iro N., 2011, MNRAS, 412, 2376
Zhou G., Bayliss D. D. R., 2012, MNRAS, 426, 2483

This paper has been typeset from a TEX/LATEX file prepared by the author.